SCIPEDIA Revista Internacional de Métodos Numéricos para Cálculo y Diseño en Ingeniería

Revista Internacional Métodos numéricos para cálculo y diseño en ingeniería RIMNI in cooperation with CIMNE

# The Sealing Failure Mechanism of Old Well Plugging Section under Thermo-Mechanical Coupling in Salt Cavern Hydrogen Storage

**Jiangshuai Wang[1,*], Bohan Zheng[1], Ru Zhang[2], Qianyu Ren[1] and Zixiao Song[1]**

[1]School of Petroleum and Natural Gas Engineering, Changzhou University, Changzhou, 213164, China

[2]Changqing Branch, China National Logging Corporation, Xi'an, 710200, China

**ABSTRACT**

To address the plugged sections of old wells in salt-cavern hydrogen storage facilities, this study establishes a three-dimensional finite element model considering fluid-solid-thermal multi-field coupling effect is established. based on the Cohesive Zone Model (CZM). The model simulates the debonding failure process at the cement plug-formation interface and investigates the effects of various gas injection scenarios, operational pressures, formation temperatures, mechanical parameters of the cement plug, and interface bonding quality on the debonding failure length. Simulation results indicate that hydrogen, compared to natural gas, is more prone to interface debonding failure and leakage. Increasing the cement plug's elastic modulus from 5 to 15 GPa reduces the debonding failure length by 10.37 m and increases the fracture propagation pressure by 2.2 MPa, demonstrating that higher elastic modulus effectively mitigates the risk of interface bonding failure. Increasing the Poisson's ratio from 0.05 to 0.20 only reduces the debonding failure length by 2.2 m and increases the fracture propagation pressure by 1.2 MPa, indicating that Poisson's ratio has minimal impact on bonding failure. Micro-annular gaps are highly sensitive to bonding quality, highlighting the need for rigorous quality control at the bonding interface. Under constant low operating pressure, minor debonding persists at the interface, but as operating pressure increases, the debonding failure length grows rapidly. Additionally, with increasing temperature, the debonding failure length gradually decreases. The research findings provide guidance for the optimization of cement slurry formulations and the underground hydrogen storage process.

**OPEN ACCESS**

**Received:** 07/04/2025

**Accepted:** 10/06/2025

**DOI**
10.23967/j.rimni.2025.10.66375

**Keywords:**
Salt cavern hydrogen storage
debonding failure length
cohesive element method
wellbore sealing integrity
numerical simulation

## 1 Introduction

With the acceleration of global energy transformation, salt cavern hydrogen storage has become a key technology with large capacity and high-pressure storage and seasonal peak shaving capacity [1–3]. As shown in Fig. 1, its underground facilities are composed of shafts and salt caverns. However, due to the high diffusion characteristics of small molecular weight and low viscosity of hydrogen, it is easy

*Correspondence: Jiangshuai Wang (wjs125126@163.com). This is an article distributed under the terms of the Creative Commons BY-NC-SA license

to leak through the weak sealing of the wellbore. Yan et al. [4] systematically analyzed the integrity detection and evaluation technology of salt cavern hydrogen storage wellbore. Ji et al. [5] analyzed the leakage path of wellbore integrity of hydrogen underground storage, and found that there were many types of wellbore integrity failure. Therefore, ensuring the integrity of the wellbore is the core of hydrogen storage safety.

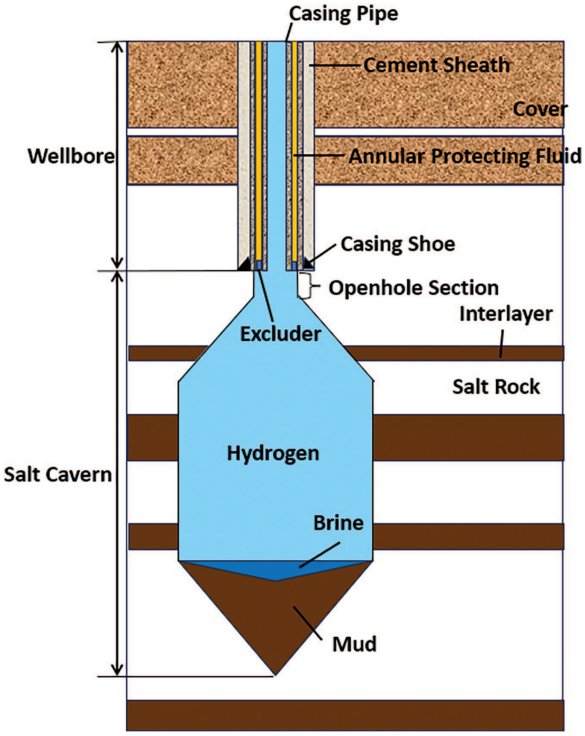


**Figure 1:** Schematic diagram of salt cavern hydrogen storage

In recent years, the mechanism of interfacial microannulus as the main channel of wellbore leakage has made important research progress [6–8]. Scholars have revealed the multi-physical field coupling mechanism of microannulus formation through theoretical modeling, numerical simulation and experimental research [9,10]. For example, Wang et al. [11] constructed a formation-cement sheath-casing-cement plug model to simulate the debonding failure process at the cement plug-casing interface. Feng et al. [12] employed cohesive elements to simulate the effect of pore pressure on debonding behavior during fluid flow. In summary, great progress has been made in the study of microannular diffusion in recent years. However, there are few studies on the simulation of cement plug-formation interface damage in the blockage section of abandoned wells in salt cavern hydrogen storage by existing models.

Over half of global gas storage leakage incidents are caused by wellbore damage [13]. Legacy brine wells (old wells) are not suitable for direct conversion into injection-production gas wells; currently, the common approach for constructing salt cavern storage is to plug the old wells with section milling and drill new wells. During high-pressure, high-frequency injection-production processes, there is still a potential risk of gas breakthrough through the cement plug itself, leading to leakage along the cement plug-formation interface (As shown in Fig. 2). Given that hydrogen has a small molecular weight and

strong escape and corrosive properties, the integrity of the sealing section in the old well of the salt cavern hydrogen storage facility must be given significant attention.

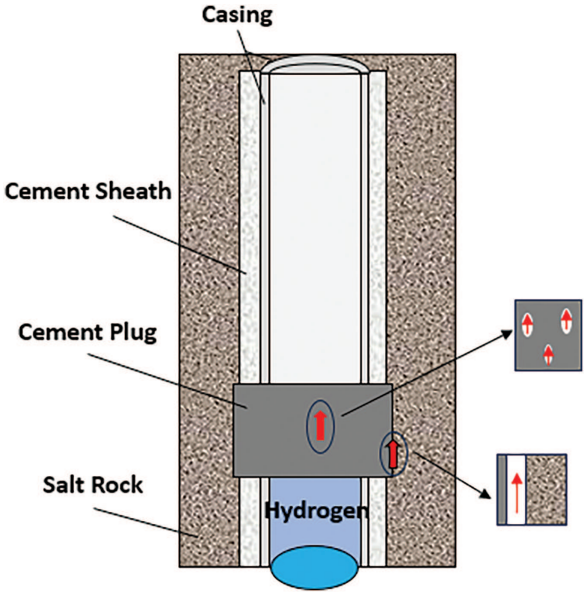


**Figure 2:** Gas leakage pathways in the sealing section of old wells

Therefore, in this paper, a three-dimensional finite element model of cement plug-formation system is established based on the Cohesive element method. The model is employed to investigate the debonding failure mechanisms of the cement plug-formation interface under various influencing factors, accompanied by a quantitative analysis of these factors. The findings provide a comprehensive understanding of the debonding behavior at the cement plug-formation interface and offer critical insights for the design and safety assessment of hydrogen storage facilities.

## 2 Governing Equations

### *2.1 Cohesive Element Method*

Fig. 3 shows a typical traction-separation response with a failure mechanism. Before reaching the stress peak value $t_n^0$, $t_s^0$ and $t_t^0$, the element exhibits elastic deformation. After exceeding the stress peak value, the element undergoes damage softening, with the corresponding effective displacement being $\delta_n^0$, $\delta_s^0$ and $\delta_t^0$. The effective displacement at complete failure is $G_C$, $\delta_s^f$ and $\delta_t^f$. The energy dissipated during this process is the fracture energy $G_C$, represented by the triangular area in Fig. 3.

The element damage is assessed based on the maximum nominal stress ratio. When the maximum nominal stress ratio in any direction reaches 1, the element undergoes initial damage, as described in [14]:

$$Max = \left\{ \frac{\langle t_n \rangle}{t_n^0}, \frac{t_s}{t_s^0}, \frac{t_t}{t_t^0} \right\} = 1 \tag{1}$$

In the equation, $t_n^0$, $t_s^0$ and $t_t^0$ represent the peak values of the nominal stress when the deformation is either purely normal to the interface or purely in the first or the second shear direction, respectively, Pa; $t_n$, $t_s$ and $t_t$ denote the stresses in the normal direction, first shear direction, and second shear direction

at the interface, Pa; The symbol ⟨⟩ represents the Macaulay bracket with the usual interpretation. The Macaulay brackets are used to signify that a pure compressive deformation or stress state does not initiate damage.

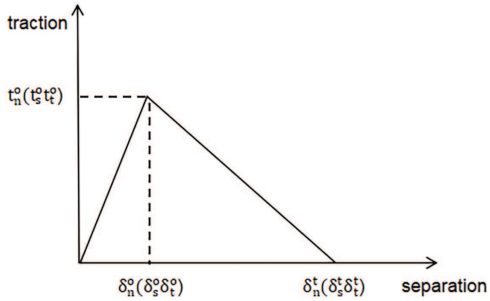


**Figure 3:** Typical traction-separation response

Fluid flow within a crack is divided into tangential flow and normal flow, as shown in Fig. 4.

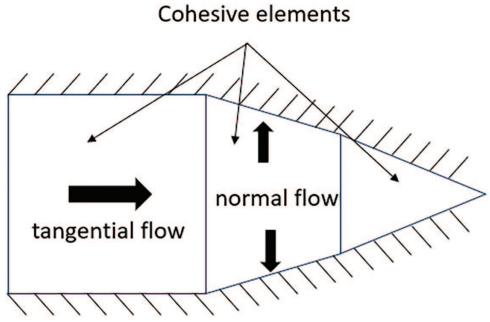


**Figure 4:** Flow in cohesive elements

The normal flow in the fracture, that is, the fluid seepage equation between the fracture surface and the formation is [15]:

$$-\frac{\partial w}{\partial t}+\nabla q+\left(\boldsymbol{q}_t+\boldsymbol{q}_b\right)=0 \tag{2}$$

In this equation, $q$ represents the tangential fluid flux, $m^2/s$; $w$ is the crack width, m; $\boldsymbol{q}_t$ and $\boldsymbol{q}_b$ are the normal filtrate velocity at the top and bottom surfaces of the crack, respectively, m/s.

Tangential flow within the crack is represented as [16]:

$$q=\frac{w^3}{12\mu_1}\nabla \boldsymbol{p}_f \tag{3}$$

In this equation, $\mu_1$ denotes the fluid viscosity, mPa·s; $\boldsymbol{p}_f$ represents the fluid pressure, Pa.

### *2.2 Thermo-Hydro-Mechanical Coupled Governing Equations*

The Thermo-hydro-mechanical coupling model describes the dynamic evolution process of the underground system by integrating the interaction mechanism of fluid motion, solid deformation and heat transfer. The specific performance is as follows: fluid migration will reconstruct the stress field of rock mass by changing the pore pressure distribution, which will lead to the dynamic adjustment

of pore structure and the reconstruction of fracture network; at the same time, the thermal convection and heat conduction between the fluid phase and the solid phase medium will drive the redistribution of the temperature field, forming a cyclic feedback mechanism of temperature-stress-seepage.

For the deformable porous media such as cement and formation, the skeleton stress equation is [17]:

$$\int_V (\bar{\sigma} - p_w I)\delta_\varepsilon \mathrm{d}V = \int_s t\delta_v \mathrm{d}S + \int_V f\delta_v \mathrm{d}V \tag{4}$$

In the formula: $\overline{\boldsymbol{\sigma}}$ is the effective stress, Pa; $\boldsymbol{p}_w$ is pore pressure, Pa; $\boldsymbol{I}$ is the unit matrix; $\boldsymbol{\delta}_\varepsilon$ is the virtual strain velocity matrix, $s^{-1}$; $\boldsymbol{\delta}_v$ virtual velocity matrix, m/s; $\boldsymbol{t}$ is the surface force per unit area, $N/m^2$; $\boldsymbol{f}$ is the physical strength per unit volume, $N/m^3$; $\mathrm{d}S$ is the area micro-element: $m^2$; $\mathrm{d}V$ is the volume element, $m^3$.

The internal seepage control equation of rock is [17]:

$$\frac{1}{J}\frac{\partial}{\partial t}(J\rho_w n_w) + \frac{\partial}{\partial x}(\rho_w n_w v_w) = 0 \tag{5}$$

In the formula: $J$ is the volume change rate of porous media; $\rho_w$ is fluid density, $kg/m^3$; $n_w$ is the void ratio; $v_w$ is the fluid seepage velocity, m/s; $x$ is the space vector, m; $t$ is the time, s.

The constitutive equation of rock considering hot pore elasticity is [18]:

$$\boldsymbol{\sigma}_{ij} = 2G\varepsilon_{ij} + \delta_{ij}\left(\lambda\varepsilon_{kk} - \frac{E\gamma\Delta T}{1-2\mu} + \alpha \boldsymbol{p}_w\right) \tag{6}$$

of which:

$$\begin{cases} G = \dfrac{E}{2(1+\mu)} \\ \lambda = \dfrac{\mu E}{(1+\mu)(1-2\mu)} \end{cases} \tag{7}$$

In the formula: $\boldsymbol{\sigma}_{ij}$ is the total stress tensor, Pa; $\varepsilon_{ij}$ is the total strain tensor; $\varepsilon_{kk}$ is the static pressure strain tensor; $G$ and $\lambda$ are Lame constants, Pa; $\gamma$ is the coefficient of thermal expansion, $°C^{-1}$; $\Delta T$ is the temperature variation, °C; $E$ is elastic modulus, Pa; $\mu$ is the Poisson's ratio; $\alpha$ is biot coefficient; $\varepsilon_{ij}$ is 1 ($i = j$) or 0 ($i \neq j$), dimensionless.

## 3 Development and Validation of the Finite Element Model

### *3.1 Model Development*

This study focuses on the cement plug sealing section of a vertical wellbore casing (see Fig. 5a). A three-dimensional geometric model of the cement plug-formation assembly was established using the Abaqus finite element software (see Fig. 5b). The overall dimensions of the model are 5 m × 5 m × 40 m, with the radius of the cement plug being 110 mm. In the model, if there are defects in the bonding interface between the bottom of the cement plug and the formation, microcracks can develop at the interface. The cement plug and the formation regions are discretized using C3D8P elements, with zero-thickness cohesive elements inserted at the interface between the cement plug and the formation. The initial damaged elements are located at the bottom of the interface. To improve computational accuracy, structured meshes and transitional mesh discretization techniques

were employed (see Fig. 5c). Additionally, both the cement plug and the formation are treated as elastic porous media, with the Mohr-Coulomb criterion adopted to evaluate yield and failure.

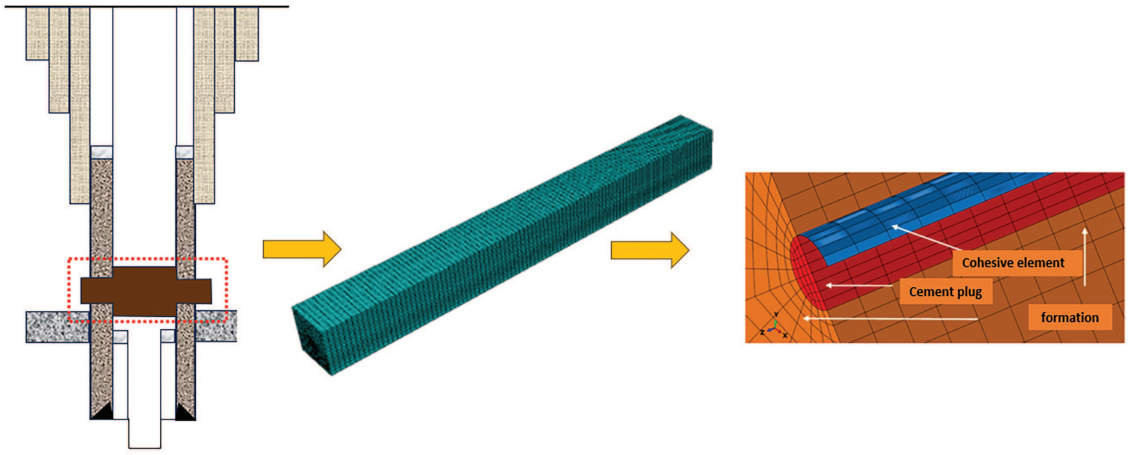


(a) research object (b) Cement plug-formation three-dimensional system (c) mesh subdivision

**Figure 5:** Research subject and cement plug-formation numerical model

A concentrated pore-flow load is applied at the bottom of the cement plug to simulate hydrogen injection and production scenarios, with an injection/production rate of 2.5 mL/s. The material properties of the model are listed in Table 1, and the interface properties of the cohesive elements are provided in Table 2. The data in Tables 1 and 2 are partially sourced from publicly available literature [19]. In addition to the specified boundary conditions, the remaining boundary constraints are as follows: (1) The boundary conditions with zero displacement are applied in the three directions of $X$, $Y$ and $Z$; (2) Applying a constant pore pressure condition corresponding to atmospheric pressure on the upper boundary; (3) Temperature load is applied to the substrate boundary. The pore pressure is 18 MPa, the maximum horizontal stress is 16.7 MPa, and the minimum horizontal stress is 10.6 MPa [20].

**Table 1:** Setting of model parameters

| Material | Elastic modulus/GPa | Poisson's ratio | Penetration/mD | Porosity |
|---|---|---|---|---|
| Cement plug | 10 | 0.10 | 0.04 | 0.28 |
| Formation | 30 | 0.20 | 4.00 | 0.18 |

**Table 2:** Cement plug-formation cementation properties

| Normal strength/MPa | Interface normal strength/MPa | Tangential strength of interface/MPa | Fracture energy/MPa·m$^{1/2}$ | Filter Loss coefficient/m·(Pa·s)$^{-1}$ |
|---|---|---|---|---|
| 0.45 | 3.15 | $8.5 \times 10^{3}$ | 1.8 | $5.3 \times 10^{-14}$ |

### *3.2 Model Validation*

Lecampion et al. [20] simulated the development process of microannulus at the cement sheath/formation interface by experimental means (Fig. 6a). Based on the experimental data, this study uses Abaqus software to establish a three-dimensional finite element model of casing-cement sheath-formation, and verifies the reliability of the modeling method through comparative analysis. The specific implementation process includes four stages: first, construct a geometric model including casing, cement sheath and formation structure; then, the constitutive relationship of each component is assigned according to the material parameters measured by the experiment. On this basis, the load conditions (including *in-situ* stress, temperature field and fluid pressure) and displacement boundary conditions consistent with the experimental conditions are applied. The simulation results are in good agreement with the experimental results, which fully verifies the effectiveness of the modeling method in characterizing the dynamic evolution process of the interface micro-annulus.

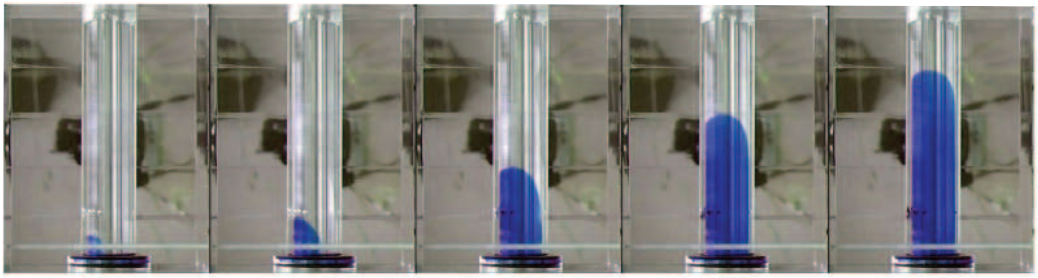

(**a**) Experimental result

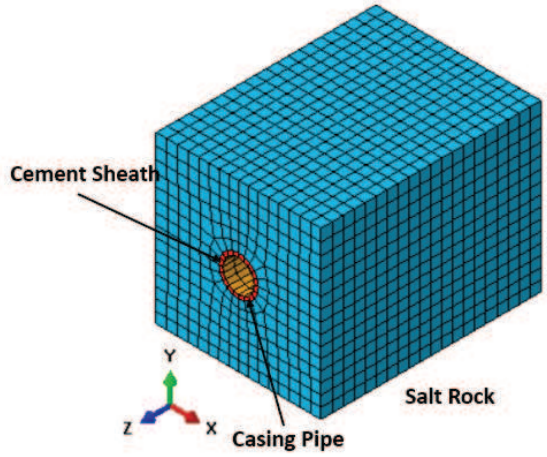


(**b**) Numerical mode

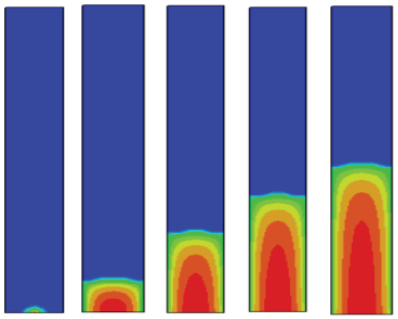

(**c**) Numerical simulation results

**Figure 6:** Experimental results and finite element simulation results of micro-cavities

## 4 Finite Element Model Results Analysis

### *4.1 Different Gas Media*

The storage of different types of gases has varying impacts on the degree of debonding damage at the cement-plug formation interface. Therefore, by altering parameters such as gas density and viscosity (as detailed in Table 3), in ABAQUS software, the characteristics of different types of gases can be simulated by adjusting the viscosity and density parameters of different gases. The influence

of the gaseous medium on the interfacial debonding failure length was investigated. The results are presented in Fig. 7a,b, where the red regions indicate areas of complete interface debonding.

As shown in Fig. 7a, the numerical model results are based on the wellbore axis. When hydrogen is stored, the debonding failure length reaches 22.45 m, which is significantly higher than 8.81 m when natural gas is stored. According to the simulation results shown in Fig. 7b, the fracture propagation pressure of hydrogen is 5.8 MPa lower than that of natural gas. This phenomenon is closely related to the molecular characteristics of hydrogen: as the smallest molecular gas, hydrogen can penetrate into the tip of the micro-crack more easily through the molecular diffusion effect, weakening the intermolecular force between the bonding surfaces of the material, thus preferentially causing interfacial debonding failure and diffusion along the micro-annulus.

**Table 3:** Gas properties

| | Density/kg·m$^{-3}$ | Viscosity/Pa·s | Flow velocity/mL/s | Initial temperature/°C | Pore pressure/MPa |
|---|---|---|---|---|---|
| $H_2$ | 0.089 | $8.76 \times 10^{-6}$ | 2.5 | 60 | 18 |
| $CH_4$ | 0.72 | $0.31 \times 10^{-4}$ | 2.5 | 60 | 18 |

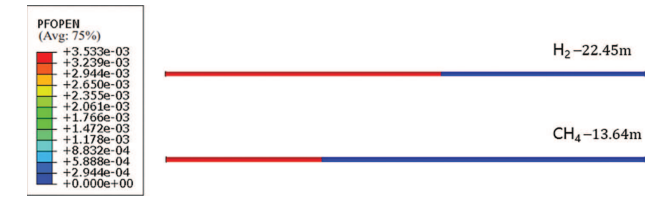


(**a**) Micro-annulus width cloud diagram under different gases

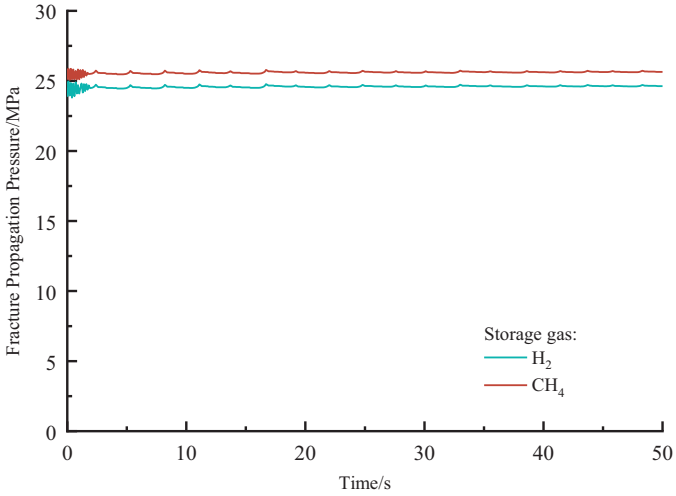


(**b**) Fracture propagation pressure under different gases

**Figure 7:** Effects of different gases on the development of microring gaps

Therefore, in the design and construction of underground hydrogen storage facilities, the specific properties of hydrogen must be carefully considered, and appropriate measures should be implemented to ensure the stability of the cement plug-formation interface. Such measures include optimizing the

cement slurry formulation to enhance its mechanical properties, and improving the monitoring and management of interface bonding quality, thereby effectively mitigating the risk of leakage.

### *4.2 Effects of Mechanical Parameters of Cement Plug*

#### *4.2.1 Elastic Modulus of Cement Plug*

Fig. 8a,b depicts the effects of the elastic modulus of the cement plug on the debonding failure length at the cement plug-formation interface and the fracture propagation pressure curves under different elastic moduli, respectively.

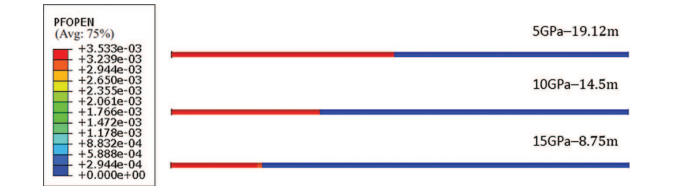


(a) Micro-annulus width cloud diagram under different elastic modulus of cement plug

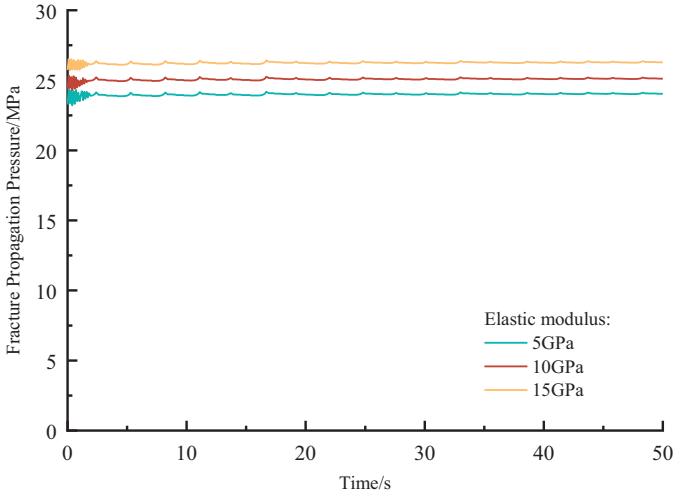


(b) Fracture propagation pressure under different elastic modulus of cement plug

**Figure 8:** Effect of elastic modulus of different cement plugs on microring development

As shown in Fig. 9, the debonding failure length at the cement plug-formation interface decreases with an increase in the elastic modulus of the cement plug. When the elastic modulus increases from 5 to 15 GPa, the debonding failure length reduces by 10.37 m, while the micro-annular gap fracture propagation pressure increases by 2.2 MPa (Fig. 10). This indicates that the elastic modulus significantly influences the debonding failure length at the cement plug-formation interface. Therefore, selecting a high-elastic-modulus cement formulation during wellbore sealing can effectively mitigate the risk of wellbore leakage.

#### *4.2.2 Cement Poisson's Ratio*

Fig. 9a,b illustrates the effects of the Poisson's ratio of the cement plug on the debonding failure length at the cement plug-formation interface and the fracture propagation pressure curves under different Poisson's ratios, respectively.


(a) Micro-annulus width cloud diagram under different cement Poisson's ratio

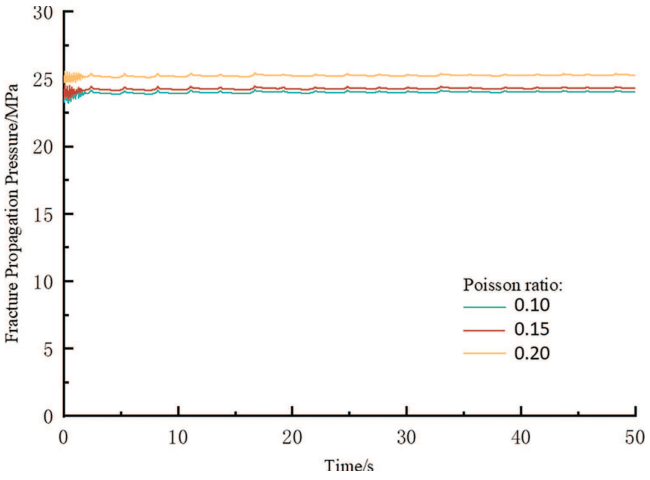


(b) Fracture propagation pressure under different cement Poisson's ratio

**Figure 9:** Effect of different cement plug porosity on microcirculation development

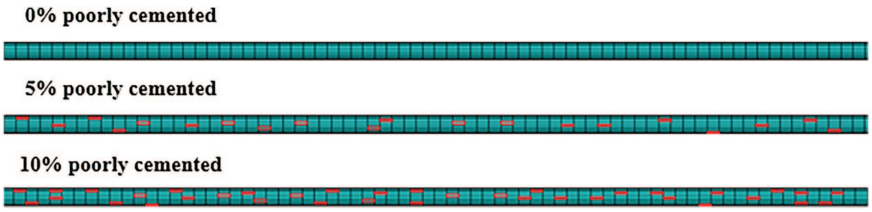


**Figure 10:** Interface cementation quality diagram

As shown in Fig. 9a, the debonding failure length at the cement plug-formation interface decreases slightly with an increase in Poisson's ratio. When the Poisson's ratio increases from 0.10 to 0.20 [15], the debonding failure length decreases by only 2.2 m, while the micro-annular gap fracture propagation pressure increases by 1.2 MPa (Fig. 9b). This indicates that Poisson's ratio has a negligible impact on the bonding failure at the cement plug-formation interface. Nevertheless, selecting a high-Poisson's-ratio cement formulation during wellbore sealing may still help reduce the risk of leakage.

### *4.3 Effects of Bonding Quality*

Residual mudcake on the wellbore wall and improper cementing operations can significantly affect bonding quality. To account for the heterogeneity and randomness of the interface bonding quality, a random sampling approach was applied to the cohesive elements. A subset of elements, designated as set A, represents poorly bonded regions (marked in red), while the remaining elements form set B, representing well-bonded regions. By varying the proportion of elements in set A, three scenarios of

bonding quality were simulated: 0%, 5%, and 10% poorly bonded regions. The sampling results are shown in Fig. 10.

As illustrated in Fig. 11a, the debonding failure length at the cement plug-formation interface increases as the poorly bonded region expands. When the proportion of poorly bonded regions increases from 0% to 10%, the debonding failure length significantly rises by 9 m, while the micro-annular gap fracture propagation pressure increases by 2.4 MPa (as shown in Fig. 11b). These findings indicate that bonding quality has a substantial impact on the debonding failure length at the cement plug-formation interface, significantly elevating the risk of wellbore leakage. It is evident that micro-annular gaps are highly sensitive to bonding quality. Therefore, strict control of the bonding quality at the interface is critical for ensuring well integrity.


(a) Micro-annulus width cloud diagram under different interface cementation quality

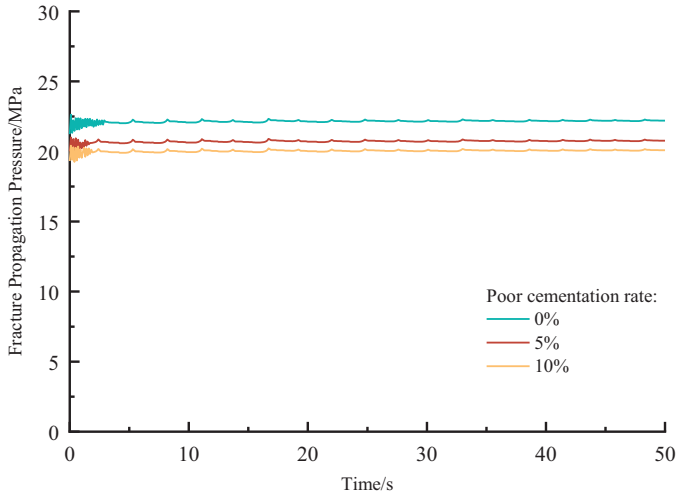


(b) Fracture propagation pressure under different interface cementation quality

**Figure 11:** The influence of different interface bonding quality on the development of microannulus

### *4.4 Effect of Operating Pressure*

Fig. 12a illustrates the effect of operating pressure on the debonding failure length at the cement plug-formation interface, while Fig. 12b presents the fracture propagation pressure curves under different operating pressures.

As shown in Fig. 12a, even under constant low operating pressure, a minor debonding phenomenon persists at the cement plug-formation interface. However, as the operating pressure increases, the debonding failure length grows rapidly. When the operating pressure increases from 7 to 22 MPa, the debonding failure length extends by 15.35 m, while the micro-annular gap fracture propagation pressure decreases by 1.9 MPa (as shown in Fig. 12b). This indicates that operating pressure significantly influences the debonding failure length at the cement plug-formation interface.

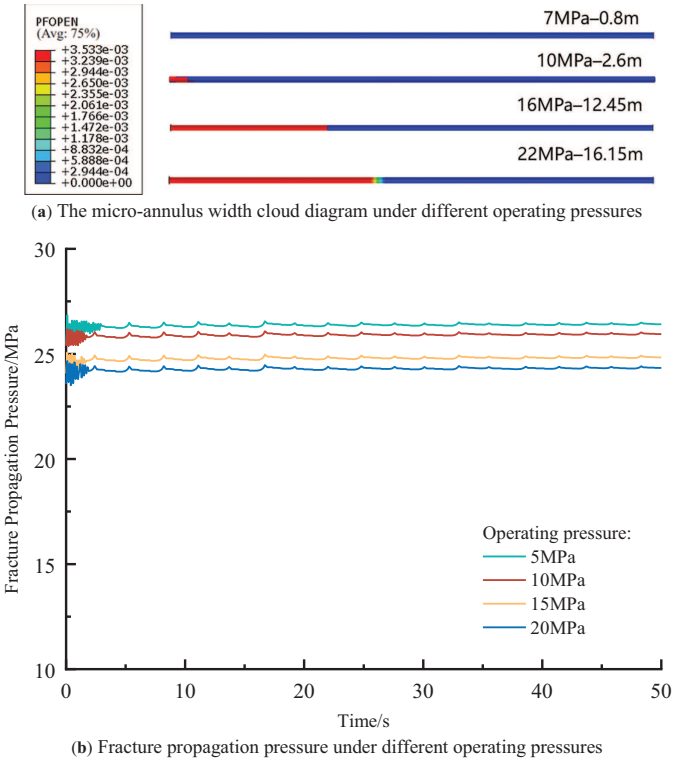


(a) The micro-annulus width cloud diagram under different operating pressures

(b) Fracture propagation pressure under different operating pressures

**Figure 12:** Effects of different operating pressures on the development of microannulus

### *4.5 Effect of Temperature Field*

This section focuses on the variation in debonding failure length at the cement plug-formation interface under different temperature conditions. In the material property settings, all external conditions remain constant except for the temperature field. Four scenarios were simulated by varying the temperature field: 0°C, 60°C, 70°C, and 80°C. Fig. 13a depicts the effect of temperature on the debonding failure length at the cement plug-formation interface, while Fig. 13b presents the fracture propagation pressure curves under different temperature conditions.

As shown in Fig. 13a, the debonding failure length at the cement plug-formation interface decreases with increasing temperature. When the temperature rises from 0°C to 80°C, the debonding failure length decreases by 7.6 m, while the micro-annular gap fracture propagation pressure increases by 1.7 MPa (Fig. 13b). This behavior is attributed to the differential expansion characteristics of the system under higher temperature conditions, which increase the compressive contact stress between the formation and the cement plug. This, in turn, enhances the bonding strength of the system and reduces the debonding failure length. Therefore, the deeper the hydrogen storage facility is buried, the deeper the cement plug sealing position, and consequently, the greater the sealing stability.

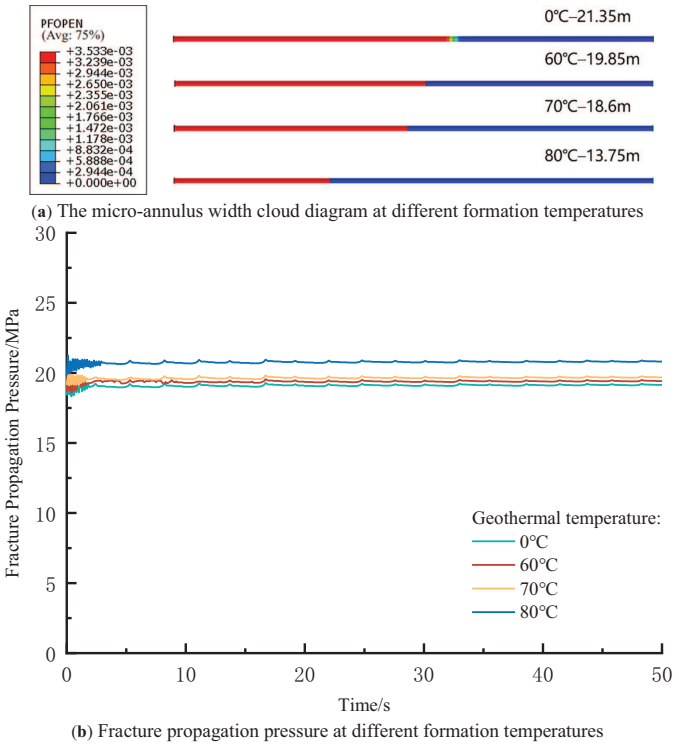


(a) The micro-annulus width cloud diagram at different formation temperatures

(b) Fracture propagation pressure at different formation temperatures

**Figure 13:** The influence of different formation temperatures on the development of microannulus

## 5 Conclusion

Using the ABAQUS software platform, a three-dimensional numerical model of the cement plug-formation system was established to simulate the debonding failure process at the cement plug-formation interface. The study investigated the effects of different gas injection scenarios, mechanical parameters of the cement plug, interface bonding quality, operating pressures, and formation temperatures on the debonding failure length at the interface. The main conclusions are as follows:

1. Under identical environmental conditions, the crack propagation pressure for hydrogen leakage is lower than that for natural gas. This indicates that the cement plug-formation interface is more prone to debonding failure during hydrogen storage.
2. When selecting cement plugs with high elastic modulus and high Poisson's ratio, the length of interface sealing failure decreases, and the crack propagation pressure increases. This reduces the risk of hydrogen leakage along abandoned wellbores. The Poisson's ratio of the cement plug has minimal impact on interface debonding failure.
3. Bonding quality significantly influences the debonding failure length at the cement plug-formation interface. Poor bonding conditions substantially increase the risk of wellbore leakage. Emphasis should be placed on ensuring high-quality bonding and minimizing areas of poor bonding.
4. Under high-pressure conditions, the debonding failure length at the cement plug-formation interface increases significantly. Conversely, as the formation temperature increases, the debonding failure length decreases.

**Acknowledgement:** Not applicable.

**Funding Statement:** This research is supported by Postgraduate Research & Practice Innovation Program of Jiangsu Province (KYCX24_3248).

**Author Contributions:** The authors confirm contribution to the paper as follows: study conception and design: Jiangshuai Wang, Bohan Zheng; data collection: Ru Zhang; analysis and interpretation of results: Qianyu Ren; draft manuscript preparation: Zixiao Song. All authors reviewed the results and approved the final version of the manuscript.

**Availability of Data and Materials:** The datasets generated and analyzed during the current study are available from the corresponding author on reasonable request.

**Ethics Approval:** Not applicable.

**Conflicts of Interest:** The authors declare no conflicts of interest to report regarding the present study.

## References

1. Ding G, Ding Y, Li Y, Tang L, Wu Z, Wanyan Q, et al. Prospects of underground gas storage in China under the strategy of carbon neutrality. Oil Gas Storage Transp. 2022;41(1):1–9. doi:10.6047/j.issn.1000-8241.2022.01.001.
2. Zou C, He D, Jia C, Xiong B, Zhao Q, Pan S. Connotation and pathway of world energy transition and its significance for carbon neutral. Acta Pet Sin. 2021;42(2):233–47. doi:10.7623/syxb202102008.
3. IEA. The future of hydrogen: seizing today's opportunities. Paris, France: IEA Publications; 2019. p. 1–7. doi:10.1787/1e0514c4-en.
4. Yan W, Leng GY, Li Z, He MQ, Deng JG, Ma ZL. Progress and challenges of underground hydrogen storage technology. Acta Pet Sin. 2023;44(3):556–68. (In Chinese).
5. Ji WD, Wan JF, He YX, Li JC, Liu W, Sun P. Key technologies and prospect of salt cavern hydrogen storage in China. Pet Drill Technol. 2024;52(4):158–66. (In Chinese).
6. Bois AP, Vu MH, Noël K, Badalamenti A, Delabroy L, Thérond E, et al. Evaluating cement-plug mechanical and hydraulic integrity. SPE Drill Complet. 2019;34(2):92–102. doi:10.2118/191335-pa.
7. Corina AN, Opedal N, Vrålstad T, Skorpa R, Sangesland S. The effect of casing-pipe roughness on cement-plug integrity. SPE Drill Complet. 2020;35(2):237–51. doi:10.2118/194158-pa.
8. Gray KE, Podnos E, Becker E. Finite-element studies of near-wellbore region during cementing operations: part I. SPE Drill Complet. 2009;24(1):127–36. doi:10.2118/106998-pa.
9. Suo Y, Chen Z, Yan H, Wang D, Zhang Y. Using cohesive zone model to simulate the hydraulic fracture interaction with natural fracture in poro-viscoelastic formation. Energies. 2019;12(7):1254. doi:10.3390/en12071254.
10. Chu W, Shen JY, Yang YF, Li Y, Gao DL. Calculation of micro-annulus size in casing-cement sheath-formation system under continuous internal casing pressure change. Pet Explor Dev. 2015;42(3):379–85. (In Chinese). doi:10.1016/s1876-3804(15)30033-1.
11. Wang JS, Cai CC. The failure law of the cement plug-casing interface for direct plugging in the casing of old wells for salt cavern gas storage. J Adhes Sci Technol. 2024;38(4):565–82. doi:10.1080/01694243.2023.2240594.
12. Feng Y, Li X, Gray KE. Development of a 3D numerical model for quantifying fluid-driven interface debonding of an injector well. Int J Greenh Gas Control. 2017;62(2):76–90. doi:10.1016/j.ijggc.2017.04.008.

13. He T, Wang T, Wang D, Xie D, Dong Z, Zhang H, et al. Integrity analysis of wellbores in the bedded salt cavern for energy storage. Energy. 2023;263(2):125841. doi:10.1016/j.energy.2022.125841.
14. Jiang J, Li J, Liu G, Lian W, Yang H. Numerical simulation of failed bonding between cement plug and casing string in abandoned wells based on cohesive element method. Drill Fluid Complet Fluid. 2020;37(3):351–7. (In Chinese). doi:10.1117/12.839044.
15. Peirce A, Detournay E. An implicit level set method for modeling hydraulically driven fractures. Comput Meth Appl Mech Eng. 2008;197(33–40):2858–85. doi:10.1016/j.cma.2008.01.013.
16. Debnath K. An introduction to advanced fluid dynamics and fluvial processes. ISH J Hydraul Eng. 2024;30(1):147–8. doi:10.1080/09715010.2023.2295003.
17. Zhang GM, Liu H, Zhang J, Wu HA, Wang XX. Three-dimensional finite element simulation and parametric study for horizontal well hydraulic fracture. J Pet Sci Eng. 2010;72(3–4):310–7. doi:10.1016/j.petrol.2010.03.032.
18. Wardeh G, Perrin B. Freezing-thawing phenomena in fired clay materials and consequences on their durability. Constr Build Mater. 2008;22(5):820–8. doi:10.1016/j.conbuildmat.2007.01.004.
19. Wang D, Li J, Liu P, Liu X, Lian W, Lu Z, et al. Simulation study of sealing integrity in abandoned wells within $CO_2$ sequestration block. Pet Drill Tech. 2023;40(3):384–90. (In Chinese). doi:10.12358/j.issn.1001-5620.2023.03.015.
20. Lecampion B, Bunger A, Kear J, Quesada D. Interface debonding driven by fluid injection in a cased and cemented wellbore: modeling and experiments. Int J Greenh Gas Control. 2013;18:208–23. doi:10.1016/j.ijggc.2013.07.012.